NANOROBOTS

Bioinspired designer DNA NanoGripper for virus sensing and potential inhibition

Lifeng Zhou[1,2]*†‡, Yanyu Xiong[1,2,3]†§, Abhisek Dwivedy[1,2,4], Mengxi Zheng[1,2,4,5], Laura Cooper[6], Skye Shepherd[2,4], Tingjie Song[1,2,5], Wei Hong[1,2,4,5], Linh T. P. Le[4,7], Xin Chen[8], Saurabh Umrao[1,2,4], Lijun Rong[6], Tong Wang[9], Brian T. Cunningham[1,2,3,4,10]*, Xing Wang[1,2,4,5,10]*

DNA has shown great biocompatibility, programmable mechanical properties, and precise structural addressability at the nanometer scale, rendering it a material for constructing versatile nanorobots for biomedical applications. Here, we present the design principle, synthesis, and characterization of a DNA nanorobotic hand, called DNA NanoGripper, that contains a palm and four bendable fingers as inspired by naturally evolved human hands, bird claws, and bacteriophages. Each NanoGripper finger consists of three phalanges connected by three rotatable joints that are bendable in response to the binding of other entities. NanoGripper functions are enabled and driven by the interactions between moieties attached to the fingers and their binding partners. We demonstrate that the NanoGripper can be engineered to effectively interact with and capture nanometer-scale objects, including gold nanoparticles, gold NanoUrchins, and SARS-CoV-2 virions. With multiple DNA aptamer nanoswitches programmed to generate a fluorescent signal that is enhanced on a photonic crystal platform, the NanoGripper functions as a highly sensitive biosensor that selectively detects intact SARS-CoV-2 virions in human saliva with a limit of detection of ~100 copies per milliliter, providing a sensitivity equal to that of reverse transcription quantitative polymerase chain reaction (RT-qPCR). Quantified by flow cytometry assays, we demonstrated that the NanoGripper-aptamer complex can effectively block viral entry into the host cells, suggesting its potential for inhibiting virus infections. The design, synthesis, and characterization of a sophisticated nanomachine that can be tailored for specific applications highlight a promising pathway toward feasible and efficient solutions to the detection and potential inhibition of virus infections.

INTRODUCTION

Machine design and manufacture have expanded into micro- and nanoscopic dimensions with more mobilities and functions through advancements in micro- and nanotechnology (*1*, *2*). In nature, the most intricate nanoscopic machines are composed of proteins and nucleic acids through bottom-up self-assembly in cellular compartments. These molecular nanomachines harness nanoscale protein dynamics to achieve defined biological functions, such as protein synthesis by the ribosome (*3*) and cargo transportation along microtubules by kinesin (*4*, *5*). Designer nanoscopic robots, or nanobots, that can effectively use external energy or stimuli to generate motions and forces that mimic natural complexes have shown remarkable potential for a variety of applications in medicine (*6*, *7*). In principle, an effective designer mechanical nanobot for biomedical applications contains rigid compartments that can host and pattern multiple external ligands for target recognition and incorporates mobile elements to grant mechanical motions to perform desired functions. At the same time, the structure must be compatible with biological analytes and environments, simple to synthesize through self-assembly, and able to maintain stability during storage and usage.

As the carrier of genetic information for most living organisms, DNA commonly stays in a ~2-nm-diameter double-helical structure that is composed of two single strands held together via Watson-Crick base pairing with a 3.4-nm length for each helical turn (*8*). These physical features make DNA an ideal molecular building block for the construction of nanoscale objects with precisely defined dimensions and curvatures (*9*). DNA nanostructures can serve as biocompatible and stable molecular pegboards in two-dimensional (2D) or 3D space with precise structural addressability to arrange external ligands, such as aptamers, peptides, proteins, and nanoparticles (NPs), into patterns with desired spacing and valency at the nanometer scale (*10*–*22*). Double-stranded DNA (dsDNA) and DNA nanostructures have also shown excellent programmable mechanical properties, making DNA a versatile material for building nanorobots for various applications (*23*, *24*).

In recent years, DNA origami technology (*20*, *25*) has proven its ability in the design and fabrication of nanoscale mechanisms and machines such as compliant mechanisms (*26*), paper origami–inspired mechanisms (*27*), and controllable nanomotors (*28*). In many of the prevailing functions, grasping is a powerful capability that a nanobot can apply to perform essential functions. However, previous studies have not achieved the design of a nanoscale mechanism made of a single origami piece that contains multiple finger-like structures radiating from a central palm to form a gripper-like complex capable of

[1]Carl R. Woese Institute for Genomic Biology, University of Illinois at Urbana-Champaign, Urbana, IL 61801, USA. [2]Holonyak Micro and Nanotechnology Lab, University of Illinois at Urbana-Champaign, Urbana, IL 61801, USA. [3]Department of Electrical and Computer Engineering, University of Illinois at Urbana-Champaign, Urbana, IL 61801, USA. [4]Department of Bioengineering, University of Illinois at Urbana-Champaign, Urbana, IL 61801, USA. [5]Department of Chemistry, University of Illinois at Urbana-Champaign, Urbana, IL 61801, USA. [6]Department of Microbiology and Immunology, College of Medicine, University of Illinois at Chicago, Chicago, IL 60612, USA. [7]VinUni-Illinois Smart Health Center, VinUniversity, Hanoi, Vietnam. [8]Center for Biophysics and Quantitative Biology, University of Illinois at Urbana-Champaign, Urbana, IL 61801, USA. [9]Advanced Science Research Center at Graduate Center, City University of New York, New York, NY 10031, USA. [10]Cancer Center at Illinois, University of Illinois at Urbana-Champaign, Urbana, IL 61801, USA.
*Corresponding author. Email: lifengzhou@pku.edu.cn (L.Z.); bcunning@illinois.edu (B.T.C.); xingw@illinois.edu (X.W.)
†These authors contributed equally to this work.
‡Present address: Department of Advanced Manufacturing and Robotics, Peking University, Beijing 100871, China.
§Present address: Department of Materials Science and Engineering, Stanford University, Stanford, CA 94305, USA.

collaboratively functioning like human fingers, for example, to grab 3D nanoscale entities such as a virus particle on one side, and that attaches the whole complex to a surface on an opposite side for biomedical applications, such as biosensing. Moreover, as demonstrated by recent studies, DNA nanostructures can be functionalized with aptamers and antibodies for the detection or inhibition of virus infections. These include the design and use of tile-based DNA nanostructures, such as DNA star (*18*, *29*) and DNA net (*30*–*32*), that we have developed for targeting dengue and severe acute respiratory syndrome coronavirus 2 (SARS-CoV-2), respectively. Origami-based DNA nanostructures can be also functionalized to trap or block viruses. For example, triangle plates assembled into icosahedral shells can trap hepatitis B virus (HBV) (*33*); cone cages showed the ability to trap influenza, SARS-CoV-2, and chikungunya (*34*); and a wireframe icosahedron can block SARS-CoV-2 entry cells (*35*). Despite the advanced designs, they cannot perform like a human hand to grasp nanometer-scale objects.

Here, we present the design, synthesis, characterization, and utility of a designer DNA nanobot named DNA NanoGripper (DNA NG or NG for short) that contains a palm and four finger-like structures inspired by naturally evolved bird claws, human hands, and bacteriophages. DNA NG is composed of a single origami piece containing four bendable fingers by adopting the classic macroscopic machine design procedure, through which adaptive ability was achieved via the incorporation of the three revolute joints to each finger. Figure 1 illustrates the schematic of NG's design, means for functionalization, and utility in viral detection and inhibition as a functional showcase. Each of the NG's fingers contains three phalanges connected by three rotatable joints. The design of the DNA NG robot is highly sophisticated because all of the static and moveable components (12 joints and 13 parts in total) are assembled as a single DNA origami piece with controlled and restricted finger-bending directions via a precise routing of the scaffold and staple strands. Functions of the NG have been enabled, and motions of the fingers have in turn been driven by the interactions between ligands attached to the fingers' surface and their binding partners. We show that the NG can be engineered to interact with or capture different nanometer-scale 3D objects with different dimensions, including gold NPs (AuNPs) and gold NanoUrchins (AuNUPs). The NG's fingers have also been functionalized to carry multiple fluorophore-labeled DNA aptamer nanoswitches (*30*, *31*) that are programmed to selectively recognize and bind intact SARS-CoV-2. Upon binding with the virus, such nanoswitches release a fluorescent signal that is subsequently enhanced when the NG-virus complexes in free solution are brought to and captured on a photonic crystal (PC) surface through DNA hybridization of complementary sequences prepared on the PC surface and the NG's palm. Through this approach, the NG successfully functions as a sensitive and specific viral biosensor on the PC surface that can detect SARS-CoV-2 virions in human saliva in 30 min with a limit of detection (LoD) of ~100 genome copies/ml, comparable to the sensitivity offered by the US Food and Drug Administration (FDA)–approved reverse transcription quantitative polymerase chain reaction (RT-qPCR) tests of 1×10^2 to 1×10^5 genome copies/ml (*36*, *37*). Furthermore, using flow cytometry assays and confocal microscopy imaging, we demonstrated that the same NG-aptamer complex can effectively block viral entry into the host cells, showing the potential of using the NG as a virus inhibitor. In summary, we report the design principle, synthesis, and characterization of a complex DNA nanobot that can be readily

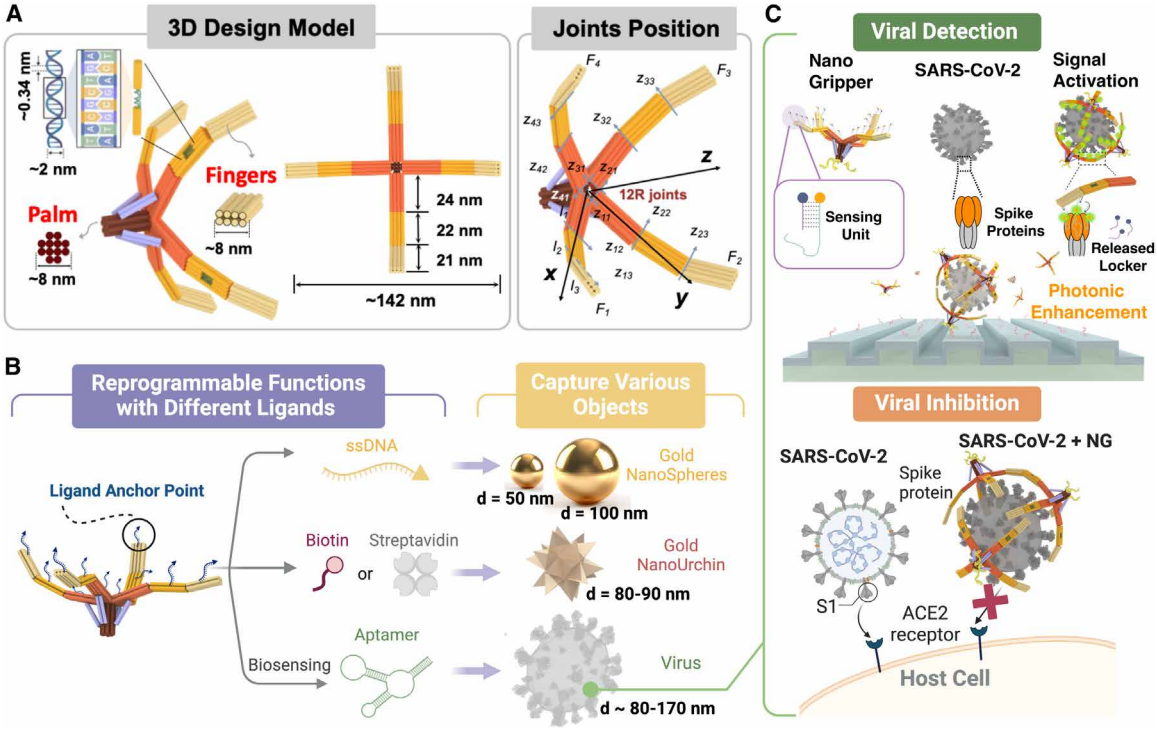

Fig. 1. Schematic of DNA NG design, functionalization, and utility in viral detection and inhibition. (**A**) Configuration and dimension of the DNA NG that contains a central palm and four bendable fingers, where *F*, *Z*, and *R* represent the finger, rotation axis and rotation joint, respectively. (**B**) Functionalization of the DNA NG for interacting with 3D nano-objects, including AuNP (~50 and 100 nm), AuNUP (~80 nm), and SARS-CoV-2 (~100 nm). "d" indicates diameter. (**C**) Schematic drawing of SARS-CoV-2 detection and cell entry inhibition using DNA NG.

tailored for rapid tests of infectious diseases caused by viruses and that may be a potential approach for blocking viral infections.

RESULTS

DNA NG design principle

Design of the DNA NG was inspired by naturally occurring analogs, such as bird claws, human hands, and bacteriophages that have evolved fingers from a central palm domain to effectively grasp objects with various matching geometries and dimensions (fig. S1A). Adopting the macroscopic machine design and manufacture procedure, the DNA NG was sculpted, synthesized, and characterized through the steps as illustrated in fig. S1B. Specifically in step 1 (nanomachine type synthesis), we decided to make an NG with four fingers by mainly considering the following three factors: (i) The human hand and most bird claws have five or three-four fingers; (ii) if one finger malfunctions in a three-finger gripper, the remaining two fingers will not function well to grab the targets; and (iii) the available scaffold DNA for making DNA origami structures is not long enough to accommodate a five-finger design with each finger still containing three phalanges connected by three flexible, human-like fingers and rotatable joints to match target dimensions. In step 2 (nanomachine dimension synthesis), our aim was for the DNA NG to easily grasp objects with an overall size of 50- to 100-nm diameter. The dimensions and parameters of the DNA NG design were determined using the method and algorithm detailed in Supplementary Methods. Accordingly in step 3 (nanomachine design analysis and optimization), we optimized the dimensions of the NG's palm [12 DNA helices cross section, 60 base pairs (bp) long] and fingers (8 DNA helices cross section, 200 bp long) on the basis of the length of the scaffold DNA (8064 bases long; see the sequence in table S1), as also illustrated in Fig. 2A and fig. S2. Furthermore,

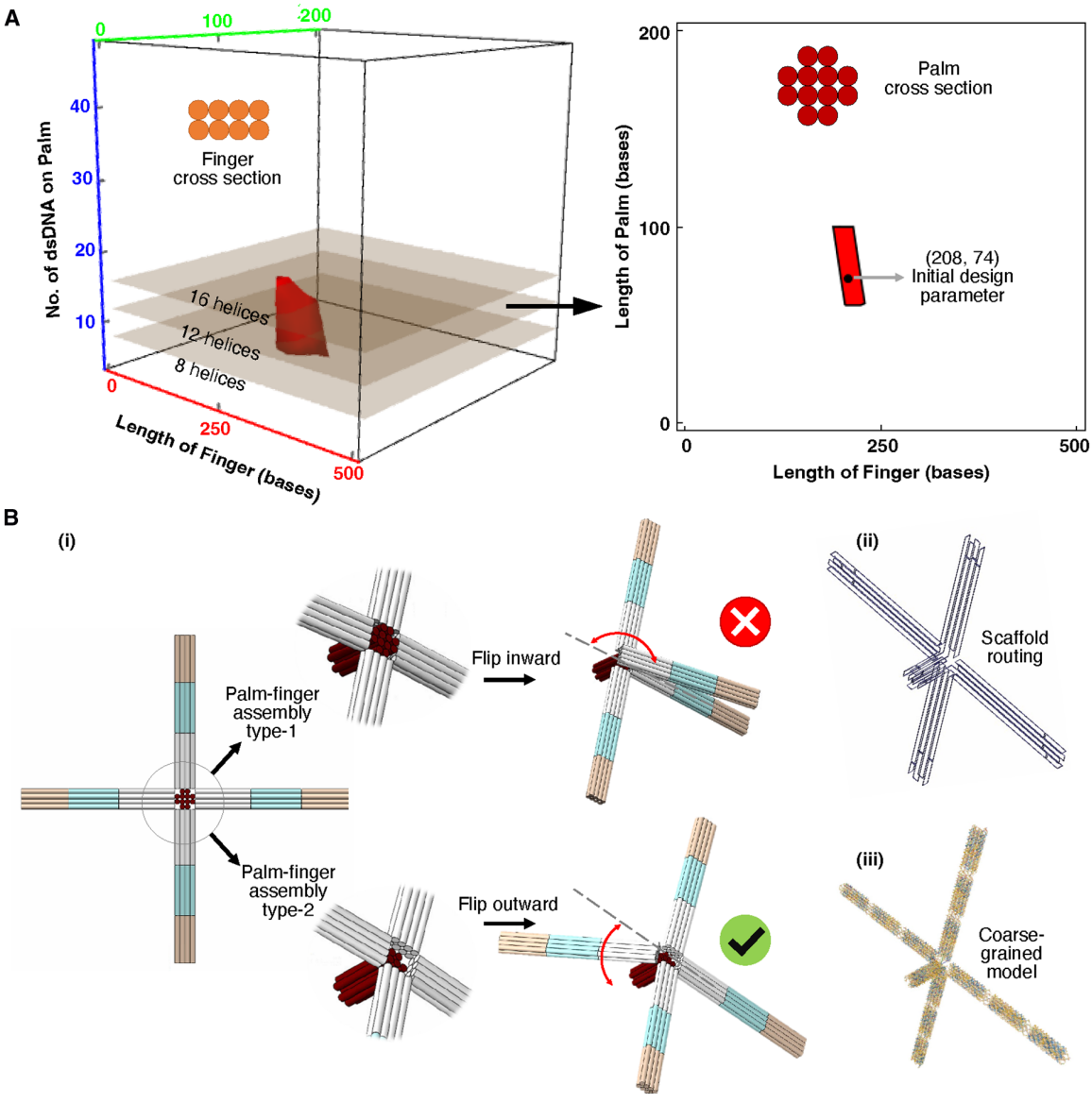

Fig. 2. DNA NG design. (**A**) Determination of optimized finger and palm cross section sizes. (**B**) Schematic of the favorite finger-palm connection design that offers an outward flip of the fingers to ensure that the NG fingers stay in open configurations in free solution (i) and schematic of scaffold DNA routing displayed using MagicDNA (ii) and oxView (iii).

all fingers were assembled above the end face of the palm to ensure that the free DNA NG stays in open configurations (Fig. 2B), as fulfilled by incorporating movable hinges on each finger with 4– to 6–nucleotide (nt)–long single-stranded DNA (ssDNA)–based hinges based on the rotational orientation of the connected dsDNA helices. In step 4 (determination of the routing of DNA origami scaffold and staples), after the dimensional design of each finger and the connection between four fingers and the palm using 4- to 6-nt-long ssDNA based on the correct rotational orientation of the connected DNA helices, we conducted the entire DNA NG design and the routing of the scaffold DNA using MagicDNA (*38*), oxView (*39*), and caDNAno (*40*), respectively (Fig. 2C, figs. S3 and S4, and movie S1). We also added dsDNA links between the palm and the fingers to constrain the bendability of the fingers and further ensure that the free DNA NG stays in its open configuration (fig. S5A). Furthermore, the oxDNA simulation demonstrated the flexible and bendable capability of the joints designed on the fingers (fig. S5B and movie S2). To enable programmable functionalities, we decorated the inward-facing surface of all four fingers with a total of 52 ssDNA overhangs extending from the staple DNA strands that can hybridize with complementary ssDNA or aptamers for grasping driven by the interactions with nanometer-scale targets (fig. S6). The scaffold DNA and all the staple DNA strands are listed in tables S1 and S2, respectively. Because our NG was designed to demonstrate its most important applications in virus sensing and potential inhibition via virus grasping (Supplementary Methods and figs. S5 and S7), we focused on the 50- to 100-nm particle size range covering many life-threatening viruses, such as coronaviruses, influenza, and HIV.

Synthesis and characterization of DNA NG

The DNA NG consisted of a long M13mp18-derived "scaffold" DNA (8064 nt long) with 229 short "staple" strands at a 1:10 molar ratio of scaffold:staple after a high- to low-temperature thermal annealing in 1× tris-acetate-ethylenediaminetetraacetic acid (TAE) buffer containing magnesium ion (Mg^{2+}) (Fig. 3A). NG formation in the buffers containing different Mg^{2+} concentrations (12 to 22 mM) was screened, and the best Mg^{2+} concentration for NG formation was determined using agarose gel electrophoresis (AGE), showing that the NG was present as the predominant species in all of the Mg^{2+}-containing buffers (Fig. 3B). However, the NG started forming higher molecular weight (MW) aggregates that failed to move beyond the wells of the gel at Mg^{2+} concentration higher than 16 mM. Thus, 1× TAE buffer containing 16 mM Mg^{2+} that provided the needed ionic strength without causing NG aggregation was used to prepare NG assemblies. Before subsequent characterization and assays, all freshly prepared NG samples were purified to remove excess staple strands by using Bio-Rad Freeze 'N squeeze DNA gel extraction spin columns or precipitation by polyethylene glycol (PEG) (*41*, *42*). The purified NG sample contained no free staples as shown by an AGE analysis (fig. S8). NG structures were visualized using atomic force microscopy (AFM) imaging (Fig. 3C-i and fig. S9) and transmission electron

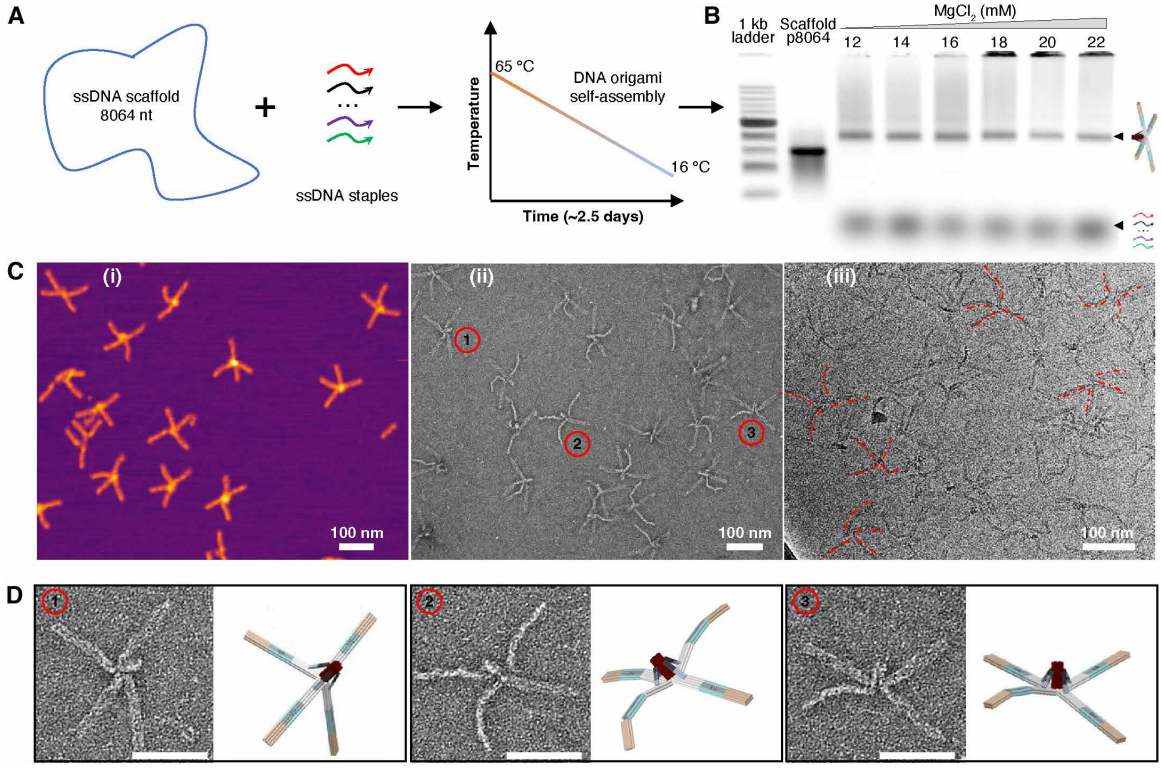

Fig. 3. Synthesis and characterization of DNA NG. (**A**) Schematic of DNA NG assembly using programmed thermal annealing. (**B**) AGE shows the NG formation (as a predominate band) in the buffer with different Mg^{2+} concentrations. All NG samples were purified to remove excess staple strands before subsequent characterization and assays. (**C**) Sample microscopy images of the DNA NG. See more AFM, TEM, and cryo-EM images of DNA NG with lower magnification in the Supplementary Materials. (i) AFM image. (ii) TEM image after negative staining. (iii) Cryo-EM image. (**D**) Side-by-side comparison of DNA NG structure obtained from TEM imaging with the corresponding NG 3D model configuration. Scale bars indicate 100 nm.

microscopy (TEM) imaging (Fig. 3C-ii and fig. S10), as projected onto 2D space with different poses that contain four bendable fingers (Fig. 3D). Furthermore, cryogenic electron microscopy (cryo-EM) images of flash-frozen NG samples were collected to show various NG poses in true 3D space (Fig. 3C-iii and fig. S11). The NG 3D structure snapshots captured by cryo-EM imaging revealed that in liquid, all of the NGs' fingers project outward from the central palm to four directions with various phalange joint angles, suggesting the potential of using NGs to capture 3D nanometer-scale objects. In addition, we assessed the stability of the DNA NG in human saliva and 10% heat-inactivated fetal bovine serum–containing cell medium, the matrices used in the virus-sensing and virus-inhibition assays, by incubating the sample at 37°C for intervals of 30, 60, and 120 min. Gel electrophoresis results indicated that the DNA NG retained its structural integrity even after 120 min of incubation in both matrices (figs. S12 and S13), confirming that the NG structure was still present when used for virus detection and inhibition assays. To confirm the function of ssDNA linkers (fig. S6) on the finger surface of the NG, we decorated the NG with streptavidin-coated quantum dots (8 nm) to showcase the NG's ability to assemble detectors on the fingers and engage diminutive particles (fig. S14).

Capture of AuNP and SARS-CoV-2 by DNA NG

We decorated the NG's fingers with ssDNA tethers or DNA aptamers (targeting the spike proteins on the SARS-CoV-2 surface) to demonstrate the potential of using NG to capture 3D nanometer-scale objects. Our AFM and TEM images showed that the NG can capture the spherical-shaped AuNPs (50- or 100-nm diameter) coated with ssDNA sequence complementary to the ssDNA tethers on NG fingers (Fig. 4A and figs. S15 and S16). We quantified the NG-AuNP complex formation with different mix ratios using AGE assays. Shown in fig. S17, all of the ssDNA-coated AuNPs formed complexes of different MWs with complementary ssDNA-carried DNA NGs when the number of NGs was highly excessive compared with the AuNPs (NG:AuNP = 24:1, 12:1, and 6:1; fig. S17, lanes 4 to 6). When more AuNPs were used to hybridize with DNA NG (NG:AuNP = 2.4:1 and 1.2:1; fig. S17, lanes 7 and 8), greater numbers of both smaller and larger MW complexes formed, as indicated by red color gel species with different mobilities from free AuNPs. The AGE data showed that NG and AuNP can form complexes with different MWs, suggesting that various numbers of NGs can patch on one AuNP in respective mixtures with different ratios of NG to AuNP. In addition, we demonstrated that the NG could not capture the AuNP when a scrambled ssDNA was decorated on the NG's fingers (fig. S18). This was also confirmed by an AGE assay (fig. S19) showing that scrambled ssDNA–carried NG and AuNPs could not form complexes as effective as those formed between DNA NG and AuNPs carrying complementary ssDNA sequences (fig. S17).

We then functionalized NG by attaching SARS-CoV-2 spike-targeting aptamers [reported in (*43*)] to enable possible capture of SARS-CoV-2 virions by NG via polyvalent aptamer-spike protein interactions (Fig. 4B). We carried out enzyme-linked immunosorbent assay (ELISA; a more reliable method) and cryo-EM imaging (spike proteins may get lost and damaged during EM sample preparation) assays to verify that the SARS-CoV-2 virions still maintained their spike proteins on the surface (fig. S20). In addition, our AGE analysis showed successful incorporation of the aptamers into the NG scaffold (fig. S21). AFM images showed that all the NG-aptamer

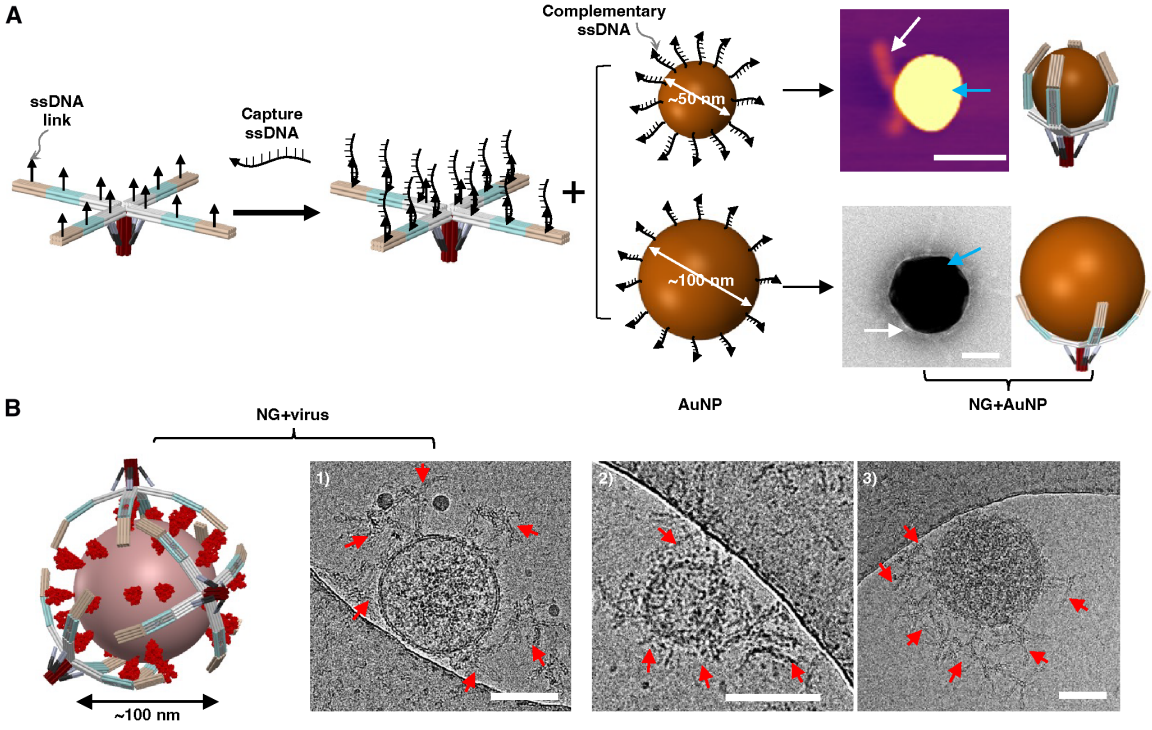

Fig. 4. Capture of AuNPs and SARS-CoV-2 by DNA NG. (**A**) AFM and TEM images show AuNPs' interaction with DNA NG carrying ssDNA with a sequence complementary to the ssDNA coated on AuNPs (50 or 100 nm). White and blue arrows indicate the NG (finger) and AuNP, respectively. Scale bars indicate 50 nm. (**B**) Cryo-EM images show the capture of SARS-CoV-2 by the DNA NG carrying multiple spike protein–targeting aptamers. Red arrows indicate the NG fingers. Scale bars indicate 50 nm.

complexes maintained their structures and stayed at open configurations (fig. S22), ensuring effective interaction with the spikes on the outer surface of the virus. As shown by the cryo-EM images in Fig. 4B, multiple NGs can adhere their fingers to the virus's outer surface with a variety of bending and binding poses because of uneven distributions of spike proteins on the surface of SARS-CoV-2. Some NGs have four fingers grasped on the viral surface, and others have fingertips touching the surface. The size of SARS-CoV-2 virus particles can vary from 50 to 180 nm (*44*). Additional cryo-EM images showed that NGs can effectively bind to the SARS-CoV-2 virus with larger diameters like ~170 nm (figs. S23 and S24). This emphasizes the NG's versatility in binding particles of different sizes, including those larger than 100 nm. To provide a more comprehensive view of the positive interactions between the NG aptamer and SARS-CoV-2, we also conducted cryo-EM tomography assays that allowed us to capture images of an NG–SARS-CoV-2 complex from different angles to offer a 3D perspective of the complex (movies S3 to S6). As a negative control, we functionalized the NG fingers with a scramble aptamer (table S3) and found that it could not capture SARS-CoV-2, as verified by the EM imaging (fig. S25). This observation confirmed the target specificity of the SARS-CoV-2 aptamer used. In summary, the effective and selective NG-virus interaction paved the way for using DNA NG for the detection and inhibition of virus infections as demonstrated hereafter using SARS-CoV-2.

On-surface capture of AuNUPs by DNA NG

Previous sections demonstrated the ability of DNA NG to grab spherical entities of various sizes, such as AuNPs via DNA hybridization or SARS-CoV-2 via aptamer-protein interactions, in a free-solution environment. Building on these foundational observations, we delved into the interactions of DNA NG with its corresponding binding targets and then immobilized DNA NG–target complex on an imaging surface for sensing. A key aspect of our investigation focused on evaluating DNA NG's capacity for digital resolution direct counting in single-molecule detection. To this end, we used AuNUP as the target, using photonic resonator absorption microscopy (PRAM) imaging as the readout detection method (*45*). This approach aimed to extend our understanding of DNA NG's capabilities from a free-solution context to a surface-anchored scenario, thereby broadening the scope of its potential applications in sensitive molecular detection. We added five ssDNA overhangs, called "anchors," to the bottom of the NG's palm, which can hybridize with the complementary "capture" ssDNAs coated on the surface of a PC biosensor for surface capture and imaging (Fig. 5A). The NG was functionalized with biotinylated ssDNAs carried on the finger surface, enabling capture of the streptavidin-coated AuNUP, and the NG-AuNUP complex was then brought onto the PC surface for imaging (Fig. 5A, see table S4 for sample preparation detail). To showcase the assays' dose response, we used PRAM to observe and count the NG-captured AuNUPs on the PC surface across different concentrations (Fig. 5B). PRAM has been developed for imaging the attachment of metallic NPs upon a PC surface, enabling the detection of NPs substantially smaller than the diffraction limits. As depicted in Fig. 5C, the metallic AuNUPs induce localized surface plasmon resonances, resulting in distinct changes (intensity reduction and wavelength shift) in the PC's resonant reflection spectrum. This effect permits the observation of individually surface-captured AuNUPs, even as small as 80 nm, using a simple and inexpensive detection instrument (*46*). As shown in Fig. 5 (B and C), the NG-captured AuNUPs from the solution at varying concentrations (0.08, 0.4, and 2 pM) were visualized and digitally counted using PRAM at different surface incubation time points (30, 60, and 90 min) after being brought onto the PC surface via anchor-capture DNA hybridization. The AuNUPs were displayed as black dots under PRAM, and the number of NG-captured AuNUPs increased over longer incubation times, which is further illustrated in Fig. 5D. Moreover, when monomeric biotinylated ssDNA (not attached to the NG's fingers) was used as a negative control probe, very few black dots were observed under PRAM because of nonspecific binding with a capture DNA-coated PC surface, which could be viewed as the detection background that appeared frequently in previous PRAM assays (*45*) (Fig. 5B). These results indicate that NGs could effectively capture targeted nanoscale entities with high sensitivity by digital counting.

Detection of SARS-CoV-2 with DNA NG sensor

After demonstrating that DNA NGs can capture and bring the binding targets in solution to a PC surface for quantification via digital counting, we reengineered DNA NG to function as a highly sensitive viral biosensor by attaching SARS-CoV-2 spike–targeting aptamer nanoswitches on the surface of the NG's fingers. As illustrated in Fig. 6A, each nanoswitch was programmed to comprise a fluorescein amidite (FAM)–labeled aptamer that partially hybridizes with a Black Hole Quencher (BHQ)–labeled "lock" DNA oligonucleotide to effectively quench the fluorescence in the absence of SARS-CoV-2 (*30*). The functional NG with aptamer-lock pairs can release a fluorescent signal only upon capturing a SARS-CoV-2 particle because the quencher oligos would be kicked out when the aptamers bind the spike proteins. Such aptamer-spike protein binding was further strengthened through multivalent interactions facilitated by the designed multiple aptamer-lock pairs on the DNA NG platform, resulting in a strong and reliable fluorescence as the detection signal. The emitted photons from released fluorescence were subsequently enhanced using a PC-enhanced fluorescence (PCEF) technology (*47*), which provided a high signal-to-noise ratio for digitally counting single emitters for ultrasensitive SARS-CoV-2 detection (Fig. 6B; see table S5 for sample preparation detail).

As dielectric microcavities, PCs can provide strong local field enhancement, far-field directional emission, substantial Purcell enhancement, and high quantum efficiency for surface-attached fluorescent reporters (*47*–*49*). Using the NG-PC hybrid system, in which the PC enhances fluorescence from unlocked reporters concentrated within anchored NGs, we reported a near–250-fold signal intensity enhancement compared with a NG reporter on a glass substrate (Fig. 6C; see the Supplementary Materials for a detailed explanation of PC-enabled fluorescence enhancement). In contrast with previously reported surface-based photonic assays (*50*, *51*), the capture of SARS-CoV-2 by NG sensors occurred quickly in solution because we intended to have a high concentration of NG in the mixture. After the capture of the viruses, the fluorescent signal was activated and subsequently enhanced when the NG-virus complexes were deposited and anchored on the functionalized PC surface through the hybridization of the anchor ssDNA at the bottom of the NG palm and the surface capture ssDNA coated on the PC surface. The enhanced fluorescence signals were displayed as white dots on the images taken by PCEF (Fig. 6D). Because of the nearly zero off-target signal achieved with this strategy, we attained an LoD of 100 copies/ml for sensing the intact virus spiked in human

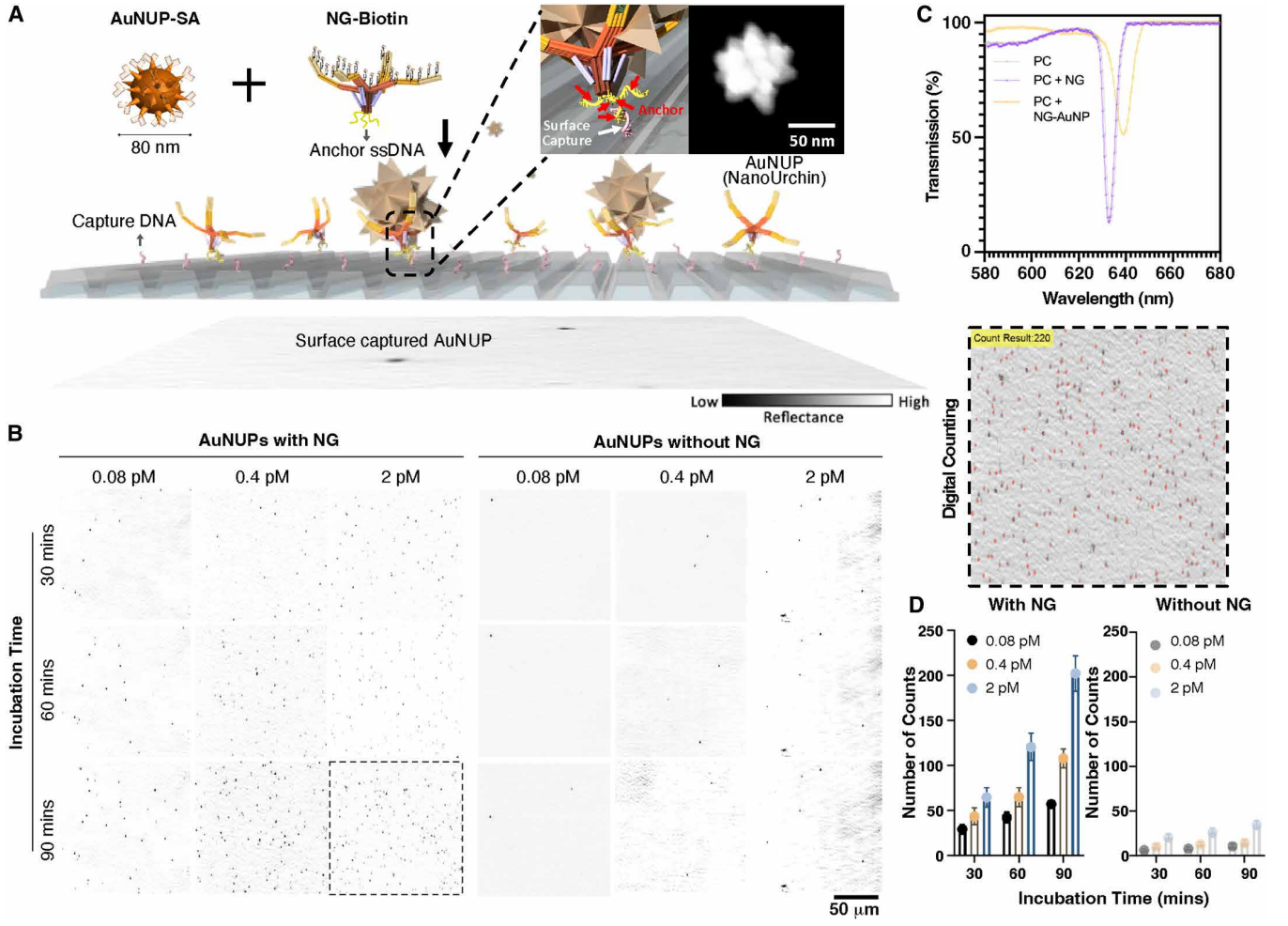

Fig. 5. Capture and count of AuNUPs on a PC surface by DNA NG. (**A**) Schematic of the capture and counting of NG-captured AuNUPs. In the zoom in subpanel, AuNUPs could be captured by NGs and then brought to the surface through the hybridization of the "Anchor" ssDNAs on the palm (indicated by red arrows) and complementary surface "capture" DNA (indicated by a white arrow) on the PC surface. NG interacts with AuNUPs via biotin-streptavidin binding. Size and shape of the AuNUPs were characterized using SEM and TEM imaging (fig. S26). (**B**) PRAM images of surface-captured AuNUPs (black dots) by DNA NGs tested at different particle concentrations and different incubation time points. Free biotinylated ssDNA (not attached to NG) was used as a negative control probe to show the background of the PC surface scan by PRAM. (**C**) Transmission scan of the PC surface in the presence or absence of surface-immobilized NGs. (**D**) Plots for the counts of surface-captured AuNUPs by DNA NGs tested at different concentrations and different incubation time points. Data are presented as mean ± SD; $n = 9$ replicates.

saliva (Fig. 6E), comparable to the sensitivity offered by the FDA-approved RT-qPCR tests of 1×10^2 to 1×10^5 copies/ml (*36*, *37*).

Although the specificity of the used aptamer had been carefully studied and tested before (*30*, *31*, *43*), we performed extra specificity tests using HIV (~100 nm) and HBV (~40 nm) as negative virus controls and found that the DNA NG–aptamer sensor designed for SARS-CoV-2 could not cross-react with HIV or HBV even at high viral loads (fig. S27, A and B). Moreover, the spike-targeting aptamer only (without NG) could not generate a detectable signal under PCEF even at a high SARS-CoV-2 concentration (fig. S27C). These data demonstrated that our NG aptamer–based biosensor is selective and that the fluorescence signal is generated only in the presence of both the NG aptamer and SARS-CoV-2.

Blocking SARS-CoV-2 viral cell entry with DNA NG

Previous studies have shown that 2D or 3D DNA nanostructures can be functionalized to latch onto the viral surface to interrupt viral cell entry by physically blocking virus-cell interactions (*18*, *29*, *30*, *33*, *34*, *52*). Our cryo-EM imaging assays have shown that multiple DNA NGs can bind to the surface of SARS-CoV-2. Thus, we hypothesized that the DNA NG could form a physical barrier between the viral particle and the host cell for potential inhibition of virus infections. To test such potential, we used flow cytometry to analyze SARS-CoV-2 infection into VeroE6 cells with or without the presence of DNA NG under various complex compositions and/or concentrations (see table S6 for sample preparation detail). Shown in fig. S28, viable single-cell events were first gated on MHCI (major histocompatibility complex I), and the MHCI-positive population was examined for viral loads using a SARS-CoV-2 spike RBD–targeting monoclonal antibody (mAb). Our fluorescence-activated cell sorting data suggest that incubating the virus with 4 nM of the NG carrying 52 spike-targeting aptamers effectively reduces the viral load on and inside the host cells as observed by a substantial

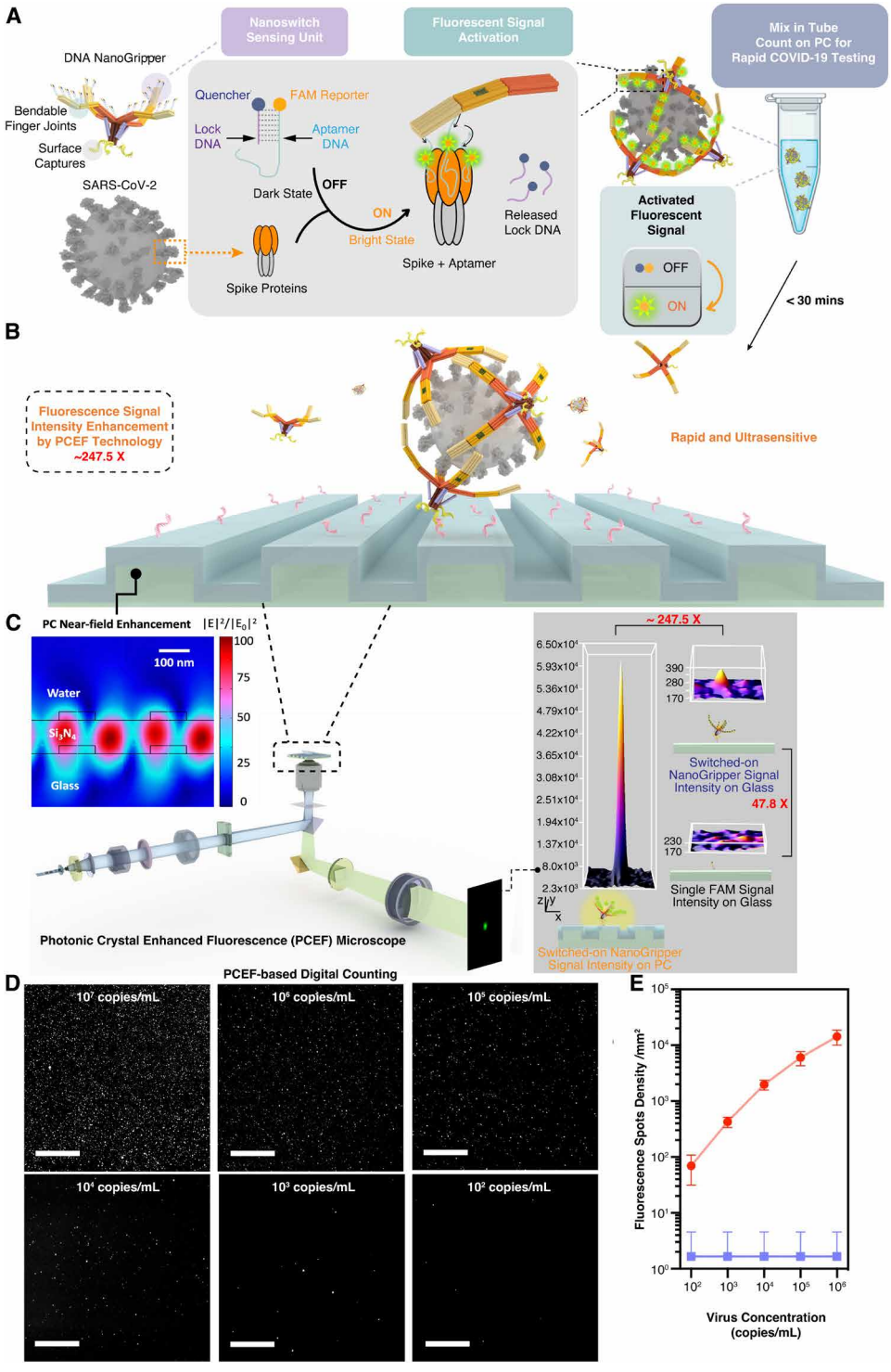

Fig. 6. PC-enhanced detection of SARS-CoV-2 by a DNA NG sensor. (**A**) Schematic of viral capture and fluorescent signal generation mechanism. (**B**) Schematic of PC-NG hybrid system shows that the NG aptamer can capture SARS-CoV-2 in free solution and then bring it to the PC surface via anchor (on NGs) and tether DNA (on PCs) hybridization. (**C**) PC near-field enhancement and PCEF scanning microscope experimentally obtained with nearly 250-fold signal enhancement compared with an NG reporter on a glass substrate. (**D**) PC-enhanced digital counting and dose response of SARS-CoV-2 detection. Representative scanning images of PC surface with captured SARS-CoV-2 at various viral concentrations (10^2 to 10^7 copies/ml) after a 10-min incubation with the NG sensor. Scale bars, 50 μm. (**E**) Quantification of captured SARS-CoV-2 virions on the PC surface at different viral concentrations. The red curve is a result of connecting the points representing the average values of the fluorescence signal counts at different virus concentrations. Assays were performed in triplicate with a similar observation. Blue baseline represents the negative controls containing only buffer solution. Error bars represent the SDs of three biologically independent measurements.

reduction in spike RBD–mAb signals (Fig. 7A). However, free aptamer with normalized concentration (208 nM = 4 nM × 52) failed to demonstrate comparable antiviral efficacy. A quantitative analysis of the median fluorescence intensity (MFI) suggested that 4 nM DNA NG with the spike-targeting aptamer reduces viral loads up to ~99%, and 0.4 nM of the same NG aptamer shows >70% antiviral efficacy (Fig. 7B). Free aptamers at matched concentrations failed to demonstrate any comparable antiviral efficacy (Fig. 7B). In addition, incubation of the virus with DNA NG or DNA NG carrying scrambled aptamers failed to reduce the viral load in host cells, suggesting that although the DNA NG provides gripping functions, the molecular interaction for recognizing SARS-CoV-2 originates from the spike-specific binding aptamer (fig. S29).

We also used confocal imaging assays to visualize that SARS-CoV-2 virions lost their cell internalization ability after being bound by DNA NG functionalized with spike protein–targeting aptamers, and the same monomeric aptamers (not attached to NG) could not effectively prevent viral cell entry (see table S7 for sample preparation detail). More specifically in our confocal assays, membrane-bound structures, including the VeroE6 cell membrane, were stained with DiD (yellow). At the same time, the cell nuclei (blue) were stained with Hoechst. SARS-CoV-2 virions were labeled with a FAM fluorophore–DNA aptamer that targets the spike proteins as a fluorescence tag for lighting up the SARS-CoV-2 virions under confocal microscopy. It also served as an aptamer-only control binder. Here, the FAM fluorophore–labeled viruses were colored as red dots during image processing. Free aptamer-only–bound or DNA NG–aptamer–bound SARS-CoV-2 virions were introduced to the stained cells for the downstream viral cell entry analysis. We then developed and implemented 3D reconstruction of collected confocal images to provide visualization-based qualitative analysis and comparison of virion entry in the presence of DNA NG–aptamer complex or monomeric aptamer control with a matched aptamer concentration (figs. S30 and S31; also see Materials and Methods for the details of our 3D confocal image reconstruction). In the free aptamer-only–bound condition (Fig. 8A and fig. S30A), a large number of SARS-CoV-2 particles accumulated in the cells over time, demonstrating that monomeric aptamers could not effectively block virus cell entry. However, in the DNA NG–aptamer–bound condition (Fig. 8B and fig. S30B), accumulation of SARS-CoV-2 in the cells was barely observed. The confocal imaging results align with the flow cytometry data, underscoring the potential of using DNA NG and its design method in developing new strategies for inhibiting viral infections.

DISCUSSION

Mechanical nanobots have garnered substantial attention in recent years given their promising potential and suitability for biological and biomedical applications. In this study, we successfully adapted the classic mechanical design art and DNA origami technology to develop a design principle and procedure for constructing a functional designer DNA NG that is inspired by the dexterity of naturally evolved human hands and bird claws with a primary function of grasping. Compared with previous efforts to design basic machinery joints/links and simple nanobots using DNA molecules (*23*, *24*), design of DNA NG is more sophisticated because all the static (palm) and moveable components (fingers), containing 12 joints and 13 parts in total, were assembled as a single DNA origami piece with controlled and restricted finger-bending direction through a precise

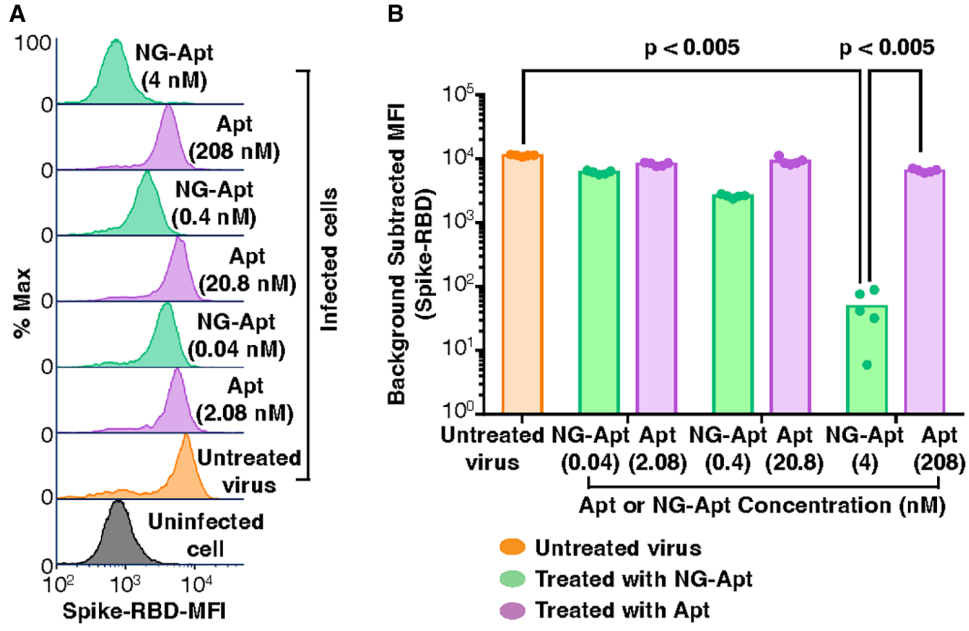

Fig. 7. Flow cytometry assay showing that the DNA NG–aptamer complex can block virus-cell interaction and virus entry with very high efficacy. (**A**) Comparative flow cytometry analysis of concentration-matched free aptamers and DNA NG–aptamer complex–mediated virus inhibition demonstrates highly effective prevention of viral entry into cells. (**B**) Viral entry into cell quantitated using intracellular staining of SARS-CoV-2 spike RBD with FITC-conjugated mAbs further demonstrates the antiviral efficacy of DNA NG–aptamer constructs. Five biological replicates were included for each condition. Statistical significance is indicated by *P* values (<0.005) as determined with unpaired two-tailed Student's *t* test. The untreated virus serves as a positive infection control (no aptamer or NG-aptamer complex added). Uninfected cell represents a negative infection control (no virus added).

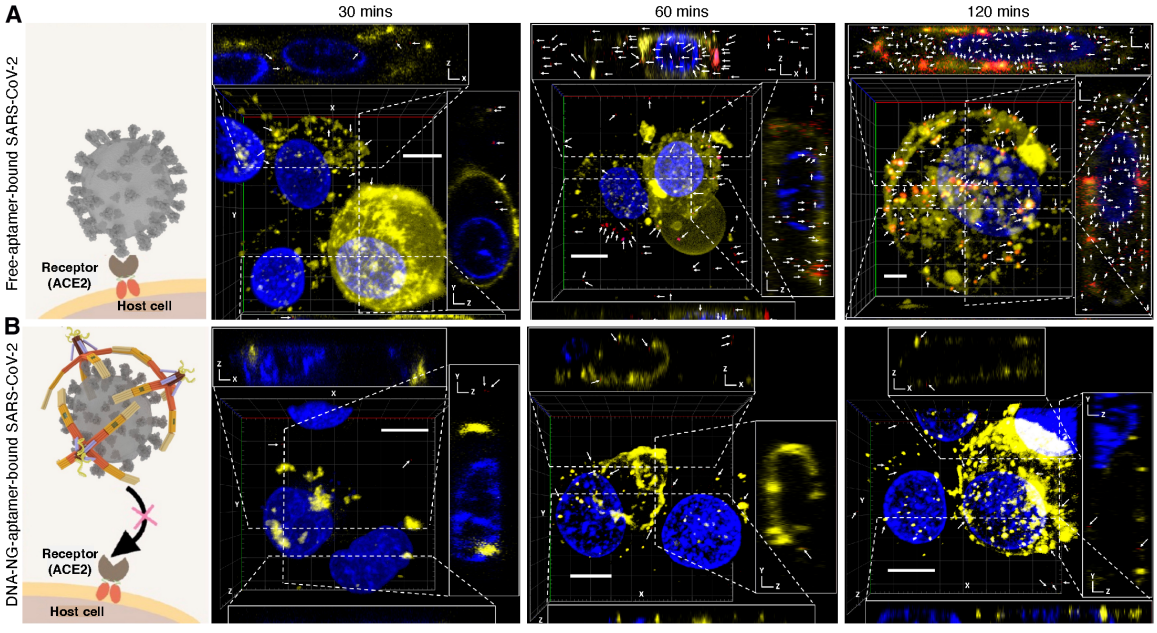

Fig. 8. SARS-CoV-2 viral cell entry inhibition by DNA NG. SARS-CoV-2 virions (red dots), VeroE6 cell membrane structures (yellow), and the cell nuclei (blue) were labeled with FAM, DiI, and Hoescht stains, respectively. Representative SARS-CoV-2 viral particles are indicated by white arrows. (**A**) SARS-CoV-2 virions accumulate in the cells over time in the presence of monomeric aptamers. A SARS-CoV-2 spike–targeting, FAM fluorophore–labeled aptamer was used as a moiety to tag the virus particles for fluorescence imaging; it also served as an aptamer-only control to provide visualization-based qualitative analysis and comparison of its antiviral function with the DNA NG aptamer–based viral inhibitor. (**B**) SARS-CoV-2 viral entry is inhibited over time by DNA NG treatment. Each panel is accompanied by three cross sections of the main view (along the dotted lines in the main images). Confocal images show that free aptamer–bound SARS-COV-2 particles accumulate in the cell (A), and DNA NG–aptamer–bound SARS-CoV-2 particles are largely prevented from cell entry (B). Assays were performed in triplicate with similar observations. Scale bars, 10 μm.

routing of the scaffold and staple strands. Specifically, our NG's fingers were designed to have relatively flexible joints with a bendable but still restricted angle ranging from 0° to 180°. Such a design ensures that the joints have a broad operational pose adaptable to interacting with particles of different sizes/surface curvatures, including the 50- to 100-nm range that we are focused on in this study to demonstrate the use cases of the NG in virus detection and inhibition. The reported design strategy involving a single origami piece also enables a much more convenient DNA nanobot sample preparation in a one-pot reaction with a higher synthetic yield. According to the classic machinery category, the NG can be classified as a parallel open-chain mechanism and is one of the most complex DNA nanomachines that has been designed to contain mobile components to date. Each NG finger is designed to contain three phalanges connected by three joints, mimicking the function of human hands or bird claws to collaboratively promote the grasp on nanometer-scale objects. As a showcase for such capabilities, we used different target recognition moieties to demonstrate that the NG can capture 50- or 100-nm AuNPs (via complementary DNA hybridization), 80-nm AuNUPs (via biotin-streptavidin binding), or approximately 100-nm intact SARS-CoV-2 virions (via aptamer–spike protein interaction). In addition, the NG served as a scaffold to carry multiple moieties to offer higher binding affinity through multivalent interaction, previously demonstrated as an effective approach to improve the target binding affinity (*18*, *29*, *30*, *33*, *34*, *52*).

The NG robot fingers were further equipped with multiple nanoswitch motifs that were transformed into a viral sensor that was programmed to release fluorescence signal only upon interacting with intact SARS-CoV-2 virions (*30*). This was achieved through the selectivity of SARS-CoV-2 spike protein–targeting aptamer and multivalent spike-aptamer interactions offered by the NG robot. After applying the NG-captured SARS-CoV-2 virion to a PC surface, the released fluorescence signal was enhanced and digitally counted by a microscope built on PCEF technology (*47*). The NG viral probe and PCEF combination gave us an LoD of 100 viral genome copies/ml in a saliva-containing solution. As a comparison, the DNA net–based virus sensors use bulk fluorescence as the detection signal readout, which suffers from high background, leading to compromised sensitivity (*30*). On the contrary, our NG-PCEF–based virus detection strategy can offer digital counting of individual virus particles specifically recognized by the NG-aptamer probe with high affinity/selectivity and imaged by PCEF with enhanced signal and minimal background, therefore improving the virus detection sensitivity such that it is comparable to the sensitivity offered by FDA-approved RT-qPCR tests of 1×10^2 to 1×10^5 genome copies/ml (*36*, *37*) and better than gold-standard antigen-based tests, such as the iHealth COVID-19 Antigen Rapid Test with an LoD of 1×10^6 to 1×10^7 copies/ml (*32*, *53*). The DNA NG probe has direct access to the intact viruses in the sample. Therefore, our SARS-CoV-2 detection approach circumvents the need for RNA extraction from the virus particles, RNA purification, reverse transcription, enzymatic amplification, and thermal cycles, resulting in a rapid and sensitive detection assay that can perform isothermally at room temperature. Our detection signal enhanced by the PCEF technology uses a standard confocal microscopy for signal readout. Thus, the assay scenario is focused on point-of-care settings. A bench-top PCEF microscopy can be built with a cost of ~$5000 when using retail parts and be much less expensive than a plate reader or real-time PCR instrument used for ELISA or RT-qPCR assay. When a portable PCEF

microscope is manufactured at a large scale, its cost is further reduced. We also estimate that the reagent and supply cost of each test is ~$1.08 (table S8), which is lower than ELISA-based antigen tests (~$5 to 10 per test) or lateral flow assay–based antigen tests (~$20 per test) (*54*). Because nucleic acid tests generate false-positive results from the presence of residual viral RNA from degraded viruses in samples (*55*, *56*), our approach, which was designed to directly sense SARS-CoV-2 virions, may also address this issue by letting people know when they are no longer infectious and can come out of quarantine.

Our study extends beyond the mechanical design of DNA NG to advance fluorescence-based biosensing. The NG's dynamic structure, with multifinger grasp ability and fluorescent signal activation, is combined with photonics metasurfaces. This integration enhances biosensing sensitivity and selectivity, addressing the limitations inherent in traditional fluorescence bioanalytical techniques. Current methods rely on the detection of ensemble analog signals from numerous labeled target molecules, which constrains the signal-to-noise ratio and detection ability. Emerging research (*57*) has shifted toward single-emitter digital counting methods to directly quantify target molecules, thereby enhancing assay sensitivity. However, this approach encounters two predominant challenges: the generation of false background counts because of nonspecific binding of fluorescent reporters and the limited binding efficiency governed by diffusion constants in surface-based reactions. Integrating with PCs, our DNA NG addresses both issues by functioning as a nanoswitch with sensing abilities. It activates fluorescent signals only upon capturing a target SARS-CoV-2, substantially reducing nonspecific binding and thus improving the LoD and accuracy. The NG capture of the target virus occurs in free solution, which is then anchored to the evanescent field-enhanced region through surface tethering, enabling single-molecule direct counting. Furthermore, our approach is augmented by the combination of specific signal activation using dynamic origami design and signal enhancement from the PC metasurface. This specifically designed PC nanostructure, serving as a versatile macroscopic substrate, harnesses specialized light-matter interactions at the nanoscale. It provides comprehensive enhancements throughout the fluorescence generation and collection processes. The signal enhancement is attributable to the multiplicative effects of enhanced excitation, highly directional extraction, and quantum efficiency improvement.

In addition to virus detection, the DNA NG aptamer has exhibited antiviral potential by wrapping the virus particles and providing a physical barrier between virus and host cell, as suggested by our EM imaging assays and in vitro SARS-CoV-2–cell entry inhibition assays. In the future, the DNA NG platform could deploy binders into various arrangements that further increase binding affinity and specificity on the basis of viral surface antigen pattern identity. Moreover, DNA NG can potentially complement the function of neutralizing antibodies (Nabs) by providing Nabs access to viral surface antigens through the uncovered regions. As demonstrated in previous studies, multivalence is used to turn a weak ligand, such as oligosaccharides (*58*), or an already strong ligand, such as a nanobody (*59*), into a stronger binder. Thus, we speculate that the DNA NG robot can provide synergy between multiple ligands and their binding targets to boost the binding affinity even for a strong binder and further improve its viral inhibitory efficacy.

In summary, by adopting the art of classic mechanical design, we have developed a design methodology/strategy for creating a highly complex but versatile DNA nanobot in a single DNA origami piece containing multiple mobile components to capture nanometer-scale objects. We developed an ultrasensitive, selective, inexpensive, single-step "direct" viral recognition platform based on DNA NG structure. The same nanobot has shown the potential for viral inhibition by physically blocking viral cell entry. Moreover, our DNA nanobot design principle can be applied to the sculpting and construction of other DNA nanomachines with desired motions and functions. Such expansion would promote the development and dissemination of DNA nanotechnology in different disciplines, triggering new and valuable interdisciplinary research topics and directions.

MATERIALS AND METHODS

Material sources

All DNA oligonucleotides were obtained from Integrated DNA Technologies (IDTDNA Inc.) and used without further purification. FAM- and BHQ1-labeled DNA oligonucleotides were purified using high-performance liquid chromatography by IDTDNA Inc. Authentic SARS-CoV-2 isolate was obtained from BEI Resources. ELISA analysis for detecting SARS-CoV-2 spike proteins was performed with a commercially available SARS-CoV-2 spike–RBD detection ELISA kit (Sino Biological KIT40592). Vero E6 cells were obtained from American Type Culture Collection (CRL-1586). Pooled human saliva was obtained from Lee Biosolution. All chemicals for making necessary buffer solutions were obtained from Sigma-Aldrich, Thermo Fisher Scientific, or VWR and sterilized using a 0.22-μm filter from Millipore. Relevant stains, dyes, and reagents were obtained from Thermo Fisher Scientific unless otherwise noted. Mica for AFM imaging was obtained from Ted Pella Inc. AFM probes (model 4XC OPUS) were obtained from MikroMasch Inc. EM grids were obtained from Electron Microscopy Sciences (catalog no. CF400-Cu). Cryo-EM grids were obtained from Ted Pella Inc. (product no. 01824).

Methods

Preparation of DNA NG structure

DNA NG was assembled in a concentration of 20 nM p8064 scaffold and 200 nM ssDNA staples in 1× TAE-Mg^{2+} (pH = 7.5) containing 40 mM tris-acetate, 2 mM EDTA, and 16 mM magnesium chloride in a 0.2-ml PCR tube (USA Scientific). Buffer was made from a 10× stock solution. The solution was annealed with the temperature gradually dropping from 65° to 16°C in about 48 hours using a thermal cycler (TProfessional TRIO PCR thermocycler) as follows: 65°C for 15 min, from 65° to 60°C for 30 min/°C, 60° to 44°C for 2.5 hours/°C, 44° to 40°C for 1 hour/°C, and 40° to 16°C for 5 min/0.1°C. After formation, DNA NG samples were stored at 4°C for short- or long-term storage for downstream assays.

AGE of DNA NG structure

The DNA NG structure was characterized with 1% AGE in 1× TAE-Mg^{2+} buffer (40 mM tris-acetate, 2 mM EDTA, pH = 7.5). We first tested 12, 14, 16, 18, 20, and 22 mM $MgCl_2$ (gel image shown in Fig. 2A); found that 16 mM works well; and then used 16 mM $MgCl_2$ for all the experiments. The gel was run at a constant voltage of 10 V/cm for 1 to 2 hours, prestained with SYBR Green (Thermo Fisher Scientific), and scanned with GelDoc (Bio-Rad).

Purification of DNA nanostructures

The DNA NG was purified using either Freeze 'N Squeeze DNA gel extraction spin columns purchased from Bio-Rad or PEG precipitation to remove excess staple strands. To purify a small scale of DNA NG with a gel extraction approach, after running an AGE, the gel

pieces were cut out from the gel slab by using a razor blade, and the NG was extracted using the Bio-Rad Freeze 'N Squeeze DNA gel extraction spin columns following the protocol provided by the manufacturer. For a larger-scale DNA NG purification, PEG precipitation was used through the following protocol. Forty nanomolars of unpurified DNA NG was mixed with an equal volume of PEG purification solution [15% PEG 8000 (w/v), 5 mM tris, 1 mM EDTA, and 505 mM NaCl]. After thorough mixing and a 5-min incubation on ice, the mixture was centrifuged at 16,000*g* at 4°C for 25 min. The supernatant was removed, and the pellet was dissolved in 1× TAE/Mg^{2+} (16 mM). The purified DNA NG sample was incubated overnight at room temperature before use. DNA NG purity was characterized using AGE to show no free staples present (fig. S8). The concentration of the purified DNA NG was measured with NanoDrop (Thermo Fisher Scientific). The formation of the purified NG was verified with AFM, TEM, and cryo-EM to ensure the structural integrity after purification. All purified NG samples were stored at 4°C before the downstream assays.

AFM imaging

3-Aminopropyltriethoxysilane (20 μl, 0.5%) was added to a freshly cleaved mica (Ted Pella Inc.) surface and incubated for 2 min to increase the adsorption of the folded DNA NG. The mica surface was then washed by ddH_2O and dried by compressed air. A drop of 5 μl of the ~2 nM purified DNA NG–containing solution was deposited onto the pretreated mica surface and incubated for 5 min. One milliliter of ddH_2O was then used to wash the mica surface and blown dry before AFM imaging. Imaging was performed under tapping mode in the air on Cypher AFM from Asylum Research with a 4XC AFM tip (OPUS, MikroMasch).

Electron microscopy

For negative staining EM experiments, we used grids that were purchased from Electron Microscopy Sciences (catalog no. CF400-Cu), which had a thin film of pure carbon (5 to 6 nm) deposited on one side of the grid. All grids with carbon side facing up were cleaned for 45 s in Fischione Nanoclean 1070 (70% power) with a mixture of argon (75%) and oxygen (25%). Five microliters of purified DNA NG (2 nM) was pipetted onto the carbon film side of a freshly cleaned grid. The sample solution was incubated on an EM grid for 3 min, and excessive solution was removed with filter paper. It was then washed with one drop of water that was removed with filter paper. Last, it was stained with 2% uranyl acetate for only 10 s. Excessive stain solution was removed with filter paper, and only a thin layer of stain solution was left on grids. EM grids were air-dried and then transferred to a desiccator for storage. EM grids were later transferred into a single tilt specimen holder that was then inserted into the microscope. Negative EM imaging was performed in either a Tecnai Spirit transmission electron microscope (Thermo Fisher Scientific) operating at 120 kV with an Eagle camera or a Titan Halo transmission electron microscope (Thermo Fisher Scientific) operating at 300 kV with a CETA camera. TEM imaging of gold NanoUrchins was done with a JEOL 2100 transmission electron microscope operating at 200 kV. Scanning electron microscopy (SEM) images of the AuNUPs were obtained using a Hitachi S-4800 field-emission scanning electron microscope. A thin conductive layer (~2 nm, gold-palladium) was sputtered onto the sample before SEM. The cryogenic transmission electron microscope experiments were performed by a 200-kV X-FEG Glacios (Thermo Fisher Scientific) with a single-particle analysis model and Thermo Fisher Scientific EPU software.

Preparation of DNA NG–authentic SARS-CoV-2 complex for cryo-EM imaging

Ten microliters of purified DNA NG (15 nM) was mixed with SARS-CoV-2 spike–targeting aptamer at a 1:52 ratio and then incubated in a thermal cycler for annealing with temperatures from 32° to 4°C for ~12 hours. Five microliters of NG-aptamer was then mixed with authentic SARS-CoV-2 (1×10^6 copies/ml) and incubated at 37°C for ~30 min before being imaged by cryo-EM.

Cryo-EM imaging

For cryo-EM experiments, we used grids that were purchased from Ted Pella Inc. (product no. 01824), which had ultrathin carbon (<3 nm) on lacey carbon support films. All grids were treated for 30 s in a Fischione model 1070 NanoClean (70% power) with a mixture of argon (75%) and oxygen (25%). Cryo-EM grids were prepared in Vitrobot (Mark IV) at 19°C with the following settings: relative humidity of 100%, wait time of 180 s, blot time of 3.5 s, and blot force of 4. Three microliters of the sample was pipetted onto a freshly glow-discharged lacey carbon grid covered with an additional thin layer of continuous carbon film. The sample solution was incubated on an EM grid for 3 min and blotted with filter paper before being plunged into liquid ethane that was precooled by liquid nitrogen. The cryo-EM grids were then transferred to and stored in liquid nitrogen. The cryo-EM grids were transferred in liquid nitrogen into a Gatan 626 cryo-specimen holder and then inserted into the microscope. The specimen temperature was maintained at −170°C during data collection. Cryo-EM imaging was done with a Titan Halo transmission electron microscope operating at 300 kV. Micrographs were recorded in the low-dose mode on a CETA camera.

Statistical analysis

The average counts of AuNUPs measured by PRAM (Fig. 5D) were measured for $n = 9$ samples at each AuNUP concentration. The average counts of the fluorescence signal detected with PCEF technology (Fig. 6E) were measured for $n = 3$ samples at each SARS-CoV-2 concentration. The average background-subtracted MFIs of spike proteins detected with RBD-targeting fluorescein isothiocyanate (FITC)–conjugated mAbs (Fig. 7B and fig. S29B) were measured for $n = 5$ samples for each antiviral construct or control. The error bars in Figs. 5D and 6E represent the SDs of the nine and three replicates, respectively. The *P* values and number of samples (*n*) are provided in the figure captions of the corresponding graphs.

Supplementary Materials

The PDF file includes:

Methods
Legends for movies S1 to S6
Figs. S1 to S31
Tables S1 to S8
References (*60*–*66*)

Other Supplementary Material for this manuscript includes the following:

Movies S1 to S6
MDAR Reproducibility Checklist

REFERENCES AND NOTES

1. C. Hu, S. Pané, B. J. Nelson, Soft micro- and nanorobotics. *Annu. Rev. Control Robot. Auton. Syst.* **1**, 53–75 (2018).
2. B. Wang, K. Kostarelos, B. J. Nelson, L. Zhang, Trends in micro–/nanorobotics: Materials development, actuation, localization, and system integration for biomedical applications. *Adv. Mater.* **33**, e2002047 (2020).

3. D. L. J. Lafontaine, D. Tollervey, The function and synthesis of ribosomes. *Nat. Rev. Mol. Cell Biol.* **2**, 514–520 (2001).
4. N. Hirokawa, Y. Noda, Y. Tanaka, S. Niwa, Kinesin superfamily motor proteins and intracellular transport. *Nat. Rev. Mol. Cell Biol.* **10**, 682–696 (2009).
5. I. Ali, W.-C. Yang, The functions of kinesin and kinesin-related proteins in eukaryotes. *Cell Adh. Migr.* **14**, 139–152 (2020).
6. C. Toumey, From nano machines to Nobel prizes. *Nat. Nanotechnol.* **12**, 1 (2017).
7. J. Li, B. Esteban-Fernández de Ávila, W. Gao, L. Zhang, J. Wang, Micro/nanorobots for biomedicine: Delivery, surgery, sensing, and detoxification. *Sci. Robot.* **2**, eaam6431 (2017).
8. J. D. Watson, F. H. C. Crick, Molecular structure of nucleic acids: A structure for deoxyribose nucleic acid. *Nature* **171**, 737–738 (1953).
9. N. C. Seeman, H. F. Sleiman, DNA nanotechnology. *Nat. Rev. Mater.* **3**, 17068 (2018).
10. Q. A. Mei, X. X. Wei, F. Y. Su, Y. Liu, C. Youngbull, R. Johnson, S. Lindsay, H. Yan, D. Meldrum, Stability of DNA origami nanoarrays in cell lysate. *Nano Lett.* **11**, 1477–1482 (2011).
11. J. Hahn, S. F. J. Wickham, W. M. Shih, S. D. Perrault, Addressing the instability of DNA nanostructures in tissue culture. *ACS Nano* **8**, 8765–8775 (2014).
12. N. P. Agarwal, M. Matthies, F. N. Gur, K. Osada, T. L. Schmidt, Block copolymer micellization as a protection strategy for DNA origami. *Angew. Chem. Int. Ed. Engl.* **56**, 5460–5464 (2017).
13. S. D. Perrault, W. M. Shih, Virus-inspired membrane encapsulation of DNA nanostructures to achieve in vivo stability. *ACS Nano* **8**, 5132–5140 (2014).
14. S. Li, Q. Jiang, S. Liu, Y. Zhang, Y. Tian, C. Song, J. Wang, Y. Zou, G. J. Anderson, J. Y. Han, Y. Chang, Y. Liu, C. Zhang, L. Chen, G. Zhou, G. Nie, H. Yan, B. Ding, Y. Zhao, A DNA nanorobot functions as a cancer therapeutic in response to a molecular trigger in vivo. *Nat. Biotechnol.* **36**, 258–264 (2018).
15. M. E. Kizer, Y. Deng, G. Kang, P. E. Mikael, X. Wang, A. J. Chung, Hydroporator: A hydrodynamic cell membrane perforator for high-throughput vector-free nanomaterial intracellular delivery and DNA origami biostability evaluation. *Lab Chip* **19**, 1747–1754 (2019).
16. D. Jiang, Z. Ge, H. J. Im, C. G. England, D. Ni, J. Hou, L. Zhang, C. J. Kutyreff, Y. Yan, Y. Liu, S. Y. Cho, J. W. Engle, J. Shi, P. Huang, C. Fan, H. Yan, W. Cai, DNA origami nanostructures can exhibit preferential renal uptake and alleviate acute kidney injury. *Nat. Biomed. Eng.* **2**, 865–877 (2018).
17. Y. Kim, P. Yin, Enhancing biocompatible stability of DNA nanostructures using dendritic oligonucleotides and brick motifs. *Angew. Chem. Int. Ed. Engl.* **59**, 700–703 (2020).
18. P. S. Kwon, S. Ren, S. J. Kwon, M. E. Kizer, L. Kuo, M. Xie, D. Zhu, F. Zhou, F. Zhang, D. Kim, K. Fraser, L. D. Kramer, N. C. Seeman, J. S. Dordick, R. J. Linhardt, J. Chao, X. Wang, Designer DNA architecture offers precise and multivalent spatial pattern-recognition for viral sensing and inhibition. *Nat. Chem.* **12**, 26–35 (2020).
19. T. Gerling, M. Kube, B. Kick, H. Dietz, Sequence-programmable covalent bonding of designed DNA assemblies. *Sci. Adv.* **4**, eaau1157 (2018).
20. P. W. Rothemund, Folding DNA to create nanoscale shapes and patterns. *Nature* **440**, 297–302 (2006).
21. A. R. Chandrasekaran, N. Anderson, M. Kizer, K. Halvorsen, X. Wang, Beyond the fold: Emerging biological applications of DNA origami. *Chembiochem* **17**, 1081–1089 (2016).
22. O. I. Wilner, I. Willner, Functionalized DNA nanostructures. *Chem. Rev.* **112**, 2528–2556 (2012).
23. J. Bath, A. J. Turberfield, DNA nanomachines. *Nat. Nanotechnol.* **2**, 275–284 (2007).
24. L. Zhou, "DNA mechanisms and machines for nanorobotics," in *Encyclopedia of Robotics*, M. H. Ang, O. Khatib, B. Siciliano, Eds. (Springer, 2021), pp. 1–12.
25. P. Zhan, A. Peil, Q. Jiang, D. Wang, S. Mousavi, Q. Xiong, Q. Shen, Y. Shang, B. Ding, C. Lin, Y. Ke, N. Liu, Recent advances in DNA origami-engineered nanomaterials and applications. *Chem. Rev.* **123**, 3976–4050 (2023).
26. L. Zhou, A. E. Marras, H.-J. Su, C. E. Castro, DNA origami compliant nanostructures with tunable mechanical properties. *ACS Nano* **8**, 27–34 (2014).
27. L. Zhou, A. E. Marras, C. M. Huang, C. E. Castro, H. J. Su, Paper origami-inspired design and actuation of DNA nanomachines with complex motions. *Small* **14**, 1802580 (2018).
28. A.-K. Pumm, W. Engelen, E. Kopperger, J. Isensee, M. Vogt, V. Kozina, M. Kube, M. N. Honemann, E. Bertosin, M. Langecker, R. Golestanian, F. C. Simmel, H. Dietz, A DNA origami rotary ratchet motor. *Nature* **607**, 492–498 (2022).
29. S. Ren, K. Fraser, L. Kuo, N. Chauhan, A. T. Adrian, F. Zhang, R. J. Linhardt, P. S. Kwon, X. Wang, Designer DNA nanostructures for viral inhibition. *Nat. Protoc.* **17**, 282–326 (2022).
30. N. Chauhan, Y. Xiong, S. Ren, A. Dwivedy, N. Magazine, L. Zhou, X. Jin, T. Zhang, B. T. Cunningham, S. Yao, W. Huang, X. Wang, Net-shaped DNA nanostructures designed for rapid/sensitive detection and potential inhibition of the SARS-CoV-2 virus. *J. Am. Chem. Soc.* **145**, 20214–20228 (2023).
31. H. Lee, W. Wang, N. Chauhan, Y. Xiong, N. Magazine, O. Valdescruz, D. Y. Kim, T. Qiu, W. Huang, X. Wang, B. T. Cunningham, Rapid detection of intact SARS-CoV-2 using designer DNA Nets and a pocket-size smartphone-linked fluorimeter. *Biosens. Bioelectron.* **229**, 115228 (2023).
32. S. Umrao, M. Zheng, X. Jin, S. Yao, X. Wang, Net-shaped DNA nanostructure-based lateral flow assays for rapid and sensitive SARS-CoV-2 detection. *Anal. Chem.* **96**, 3291–3299 (2024).
33. C. Sigl, E. M. Willner, W. Engelen, J. A. Kretzmann, K. Sachenbacher, A. Liedl, F. Kolbe, F. Wilsch, S. A. Aghvami, U. Protzer, M. F. Hagan, S. Fraden, H. Dietz, Programmable icosahedral shell system for virus trapping. *Nat. Mater.* **20**, 1281–1289 (2021).
34. A. Monferrer, F. Kohler, C. Sigl, M. Schachtner, D. Peterhoff, B. Asbach, R. Wagner, H. Dietz, DNA origami traps for large viruses. *Cell Rep. Phys. Sci.* **4**, 101237 (2023).
35. J. Zhang, Y. Xu, Y. Huang, M. Sun, S. Liu, S. Wan, H. Chen, C. Yang, Y. Yang, Y. Song, Spatially patterned neutralizing icosahedral DNA nanocage for efficient SARS-CoV-2 blocking. *J. Am. Chem. Soc.* **144**, 13146–13153 (2022).
36. US Food and Drug Administration, "SARS-CoV-2 reference panel comparative data" (2020); https://public4.pagefreezer.com/browse/FDA/17-05-2021T12:50/https://www.fda.gov/medical-devices/coronavirus-covid-19-and-medical-devices/sars-cov-2-reference-panel-comparative-data.
37. K. T. Tuzman, "Harmonizing limits of detection for FDA-authorized COVID-19 diagnostics" (BioCentury, 2020); https://www.biocentury.com/article/630429/harmonizing-limits-of-detection-for-fda-authorized-covid-19-diagnostics.
38. C.-M. Huang, A. Kucinic, J. A. Johnson, H.-J. Su, C. E. Castro, Integrated computer-aided engineering and design for DNA assemblies. *Nat. Mater.* **20**, 1264–1271 (2021).
39. E. Poppleton, J. Bohlin, M. Matthies, S. Sharma, F. Zhang, P. Šulc, Design, optimization and analysis of large DNA and RNA nanostructures through interactive visualization, editing and molecular simulation. *Nucleic Acids Res.* **48**, e72 (2020).
40. S. M. Douglas, A. H. Marblestone, S. Teerapittayanon, A. Vazquez, G. M. Church, W. M. Shih, Rapid prototyping of 3D DNA-origami shapes with caDNAno. *Nucleic Acids Res.* **37**, 5001–5006 (2009).
41. K. F. Wagenbauer, F. A. S. Engelhardt, E. Stahl, V. K. Hechtl, P. Stömmer, F. Seebacher, L. Meregalli, P. Ketterer, T. Gerling, H. Dietz, How we make DNA origami. *Chembiochem* **18**, 1873–1885 (2017).
42. C. E. Castro, F. Kilchherr, D. N. Kim, E. L. Shiao, T. Wauer, P. Wortmann, M. Bathe, H. Dietz, A primer to scaffolded DNA origami. *Nat. Methods* **8**, 221–229 (2011).
43. Y. Song, J. Song, X. Wei, M. Huang, M. Sun, L. Zhu, B. Lin, H. Shen, Z. Zhu, C. Yang, Discovery of aptamers targeting the receptor-binding domain of the SARS-CoV-2 spike glycoprotein. *Anal. Chem.* **92**, 9895–9900 (2020).
44. S. Krasemann, C. Dittmayer, S. von Stillfried, J. Meinhardt, F. Heinrich, K. Hartmann, S. Pfefferle, E. Thies, R. von Manitius, T. A. D. Aschman, J. Radke, A. Osterloh, S. Schmid, E. M. Buhl, J. Ihlow, F. Dubois, V. Arnhold, S. Elezkurtaj, D. Horst, A. Hocke, S. Timm, S. Bachmann, V. Corman, H.-H. Goebel, J. Matschke, S. Stanelle-Bertram, G. Gabriel, D. Seilhean, H. Adle-Biassette, B. Ondruschka, M. Ochs, W. Stenzel, F. L. Heppner, P. Boor, H. Radbruch, M. Laue, M. Glatzel, Assessing and improving the validity of COVID-19 autopsy studies - A multicentre approach to establish essential standards for immunohistochemical and ultrastructural analyses. *EBioMedicine* **83**, 104193 (2022).
45. T. D. Canady, N. Li, L. D. Smith, Y. Lu, M. Kohli, A. M. Smith, B. T. Cunningham, Digital-resolution detection of microRNA with single-base selectivity by photonic resonator absorption microscopy. *Proc. Natl. Acad. Sci. U.S.A.* **116**, 19362–19367 (2019).
46. Y. Zhuo, H. Hu, W. L. Chen, M. Lu, L. M. Tian, H. J. Yu, K. D. Long, E. Chow, W. P. King, S. Singamaneni, B. T. Cunningham, Single nanoparticle detection using photonic crystal enhanced microscopy. *Analyst* **139**, 1007–1015 (2014).
47. Y. Xiong, Q. Huang, T. D. Canady, P. Barya, S. Liu, O. H. Arogundade, C. M. Race, C. Che, X. Wang, L. Zhou, X. Wang, M. Kohli, A. M. Smith, B. T. Cunningham, Photonic crystal enhanced fluorescence emission and blinking suppression for single quantum dot digital resolution biosensing. *Nat. Commun.* **13**, 4647 (2022).
48. Y. Xiong, S. Shepherd, J. Tibbs, A. Bacon, W. Liu, L. D. Akin, T. Ayupova, S. Bhaskar, B. T. Cunningham, Photonic crystal enhanced fluorescence: A review on design strategies and applications. *Micromachines* **14**, 668 (2023).
49. Y. Xiong, N. Li, C. Che, W. Wang, P. Barya, W. Liu, L. Liu, X. Wang, S. Wu, H. Hu, B. T. Cunningham, Microscopies enabled by photonic metamaterials. *Sensors* **22**, 1086 (2022).
50. N. Li, X. Wang, J. Tibbs, C. Che, A. S. Peinetti, B. Zhao, L. Liu, P. Barya, L. Cooper, L. Rong, X. Wang, Y. Lu, B. T. Cunningham, Label-free digital detection of intact virions by enhanced scattering microscopy. *J. Am. Chem. Soc.* **144**, 1498–1502 (2022).
51. P. Barya, Y. Xiong, S. Shepherd, R. Gupta, L. D. Akin, J. Tibbs, H. Lee, S. Singamaneni, B. T. Cunningham, Photonic-plasmonic coupling enhanced fluorescence enabling digital-resolution ultrasensitive protein detection. *Small* **19**, 2370370 (2023).
52. A. Monferrer, J. A. Kretzmann, C. Sigl, P. Sapelza, A. Liedl, B. Wittmann, H. Dietz, Broad-spectrum virus trapping with heparan sulfate-modified DNA origami shells. *ACS Nano* **16**, 20002–20009 (2022).
53. iHealth COVID-19 Antigen Rapid Test; https://ihealthlabs.com/products/ihealth-covid-19-antigen-rapid-test.
54. A. Biby, X. Wang, X. Liu, O. Roberson, A. Henry, X. Xia, Rapid testing for coronavirus disease 2019 (COVID-19). *MRS Commun.* **12**, 12–23 (2022).

55. Korea Centers for Disease Control and Prevention, "Findings from investigation and analysis of re-positive cases" (19 May 2020); https://www.kdca.go.kr/upload_comm/syview/doc.html?fn=159118745823700.pdf&rs=/upload_comm/docu/0030/.
56. J. Lu, J. Peng, Q. Xiong, Z. Liu, H. Lin, X. Tan, M. Kang, R. Yuan, L. Zeng, P. Zhou, C. Liang, L. Yi, L. du Plessis, T. Song, W. Ma, J. Sun, O. G. Pybus, C. Ke, Clinical, immunological and virological characterization of COVID-19 patients that test re-positive for SARS-CoV-2 by RT-PCR. *EBioMedicine* **59**, 102960 (2020).
57. Q. Huang, N. Li, H. Zhang, C. Che, F. Sun, Y. Xiong, T. D. Canady, B. T. Cunningham, Critical review: Digital resolution biomolecular sensing for diagnostics and life science research. *Lab Chip* **20**, 2816–2840 (2020).
58. S. J. Kwon, D. H. Na, J. H. Kwak, M. Douaisi, F. Zhang, E. J. Park, J. H. Park, H. Youn, C. S. Song, R. S. Kane, J. S. Dordick, K. B. Lee, R. J. Linhardt, Nanostructured glycan architecture is important in the inhibition of influenza A virus infection. *Nat. Nanotechnol.* **12**, 48–54 (2017).
59. M. Schoof, B. Faust, R. A. Saunders, S. Sangwan, V. Rezelj, N. Hoppe, M. Boone, C. B. Billesbølle, C. Puchades, C. M. Azumaya, H. T. Kratochvil, M. Zimanyi, I. Deshpande, J. Liang, S. Dickinson, H. C. Nguyen, C. M. Chio, G. E. Merz, M. C. Thompson, D. Diwanji, K. Schaefer, A. A. Anand, N. Dobzinski, B. S. Zha, C. R. Simoneau, K. Leon, K. M. White, U. S. Chio, M. Gupta, M. Jin, F. Li, Y. Liu, K. Zhang, D. Bulkley, M. Sun, A. M. Smith, A. N. Rizo, F. Moss, A. F. Brilot, S. Pourmal, R. Trenker, T. Pospiech, S. Gupta, B. Barsi-Rhyne, V. Belyy, A. W. Barile-Hill, S. Nock, Y. Liu, N. J. Krogan, C. Y. Ralston, D. L. Swaney, A. García-Sastre, M. Ott, M. Vignuzzi, QCRG Structural Biology Consortium, P. Walter, A. Manglik, An ultrapotent synthetic nanobody neutralizes SARS-CoV-2 by stabilizing inactive spike. *Science* **370**, 1473–1479 (2020).
60. T. Song, H. Liang, Synchronized assembly of gold nanoparticles driven by a dynamic DNA-fueled molecular machine. *J. Am. Chem. Soc.* **134**, 10803–10806 (2012).
61. T. Bepler, K. Kelley, A. J. Noble, B. Berger, Topaz-Denoise: General deep denoising models for cryoEM and cryoET. *Nat. Commun.* **11**, 5208 (2020).
62. A. Thielens, E. Vivier, F. Romagné, NK cell MHC class I specific receptors (KIR): From biology to clinical intervention. *Curr. Opin. Immunol.* **24**, 239–245 (2012).
63. A. Sengar, T. E. Ouldridge, O. Henrich, L. Rovigatti, P. Šulc, A primer on the oxDNA model of DNA: When to use it, how to simulate it and how to interpret the results. *Front. Mol. Biosci.* **8**, 693710 (2021).
64. B. E. K. Snodin, F. Randisi, M. Mosayebi, P. Šulc, J. S. Schreck, F. Romano, T. E. Ouldridge, R. Tsukanov, E. Nir, A. A. Louis, J. P. K. Doye, Introducing improved structural properties and salt dependence into a coarse-grained model of DNA. *J. Chem. Phys.* **142**, 234901 (2015).
65. J. Bohlin, M. Matthies, E. Poppleton, J. Procyk, A. Mallya, H. Yan, P. Šulc, Design and simulation of DNA, RNA and hybrid protein–nucleic acid nanostructures with oxView. *Nat. Protoc.* **17**, 1762–1788 (2022).
66. T. Song, L. Cooper, J. Galván Achi, X. Wang, A. Dwivedy, L. Rong, X. Wang, Polyvalent nanobody structure designed for boosting SARS-CoV-2 inhibition. *J. Am. Chem. Soc.* **146**, 5894–5900 (2024).

Acknowledgments: We acknowledge the Imaging Facility of Advanced Science Research Center at GC of CUNY, the Electron Microscopy cores at the Materials Research Laboratory (MRL) at UIUC, and the Imaging Cores at the Carl R. Woese Institute for Genomic Biology (IGB) for the technical assistance. **Funding:** This work was supported in part by grants from NIH R21EB031310 (to X.W. and B.T.C.), NIH R44DE030852 (to X.W.), NIH R21AI166898 (to X.W.), NSF-CBET 19–00277 (to B.T.C.), UIUC IGB Fellowship (to L.Z.), and C*STAR Fellowship from the Cancer Center at Illinois (to Y.X.). **Author contributions:** Conceptualization: L.Z., X.W., Methodology: L.Z., Y.X., A.D., M.Z., L.C., S.S., T.S., W.H., L.T.P.L., X.C., S.U., L.R., B.T.C., and X.W. Validation: L.Z., Y.X., A.D., M.Z., L.C., S.S., T.S., W.H., L.T.P.L., X.C., S.U., L.R., B.T.C., and X.W. Formal analysis: L.Z., Y.X., A.D., M.Z., L.C., S.S., T.S., W.H., L.T.P.L., X.C., S.U., L.R., B.T.C., and X.W. Investigation: L.Z., Y.X., A.D., M.Z., L.C., S.S., T.S., W.H., L.T.P.L., X.C., and S.U. Resources: L.R., T.W., B.T.C., and X.W. Data curation: L.Z., Y.X., A.D., M.Z., L.C., S.S., T.S., W.H., L.T.P.L., X.C., S.U., L.R., B.T.C., and X.W. Writing–original draft: L.Z., Y.X., and X.W. Writing–review and editing: L.Z., Y.X., A.D., M.Z., L.C., S.S., T.S., W.H., L.T.P.L., X.C., S.U., L.R., T.W., B.T.C., and X.W. Supervision: X.W. Project administration: L.Z., B.T.C., and X.W. Funding acquisition: B.T.C. and X.W. **Competing interests:** DNA NG and DNA NG–aptamer constructs are available from X.W. at the University of Illinois Urbana-Champaign under a material transfer agreement with the University/Institution. A US provisional patent will be submitted based on the DNA NG part of the study reported in this manuscript by L.Z. and X.W. B.T.C. is an inventor on two patents that cover the invention and application of the PRAM (patent number 11041187, date of patent 22 June 2021; and patent number: 11591640, date of patent 28 February 2023). B.T.C. is a co-founder of Atzeyo Biosensors, a start-up company that licensed PRAM patents with a license option agreement. The other authors declare that they have no competing interests. **Data and materials availability:** All data needed to evaluate the conclusions in the paper are present in the paper or the Supplementary Materials. The datasets for the plots (Figs. 5, C and D; 6, C and E; and 7B) in this study have been deposited at https://doi.org/10.6084/m9.figshare.c.7508712.

Submitted 11 April 2023
Accepted 25 October 2024
Published 27 November 2024
10.1126/scirobotics.adi2084